The promoting role of Ag in Ni-CeO$_2$ catalyzed CH$_4$-CO$_2$ dry reforming reaction

Mingjue Yu [a], Yi-An Zhu [a], Yong Lu [b], Gangsheng Tong [c], Kake Zhu [a,*], Xinggui Zhou [a]

[a] UNILAB, State Key Lab of Chemical Engineering, School of Chemical Engineering, East China University of Science and Technology, 130 Meilong Road, Shanghai 200237, PR China
[b] Shanghai Key Laboratory of Green Chemistry and Chemical Processes, Department of Chemistry, East China Normal University, Shanghai 200062, PR China
[c] Instrumental Analysis Center, Shanghai Jiao Tong University, 800 Dongchuan Road, Shanghai 200240, PR China

## A R T I C L E   I N F O

A B S T R A C T

The catalytic performance of Ag promoted Ni/CeO$_2$ catalyst has been investigated in methane and carbon dioxide dry reforming reaction. The temperature-dependent catalytic activity and time-on-stream catalytic performance at 760 °C under different feeding conditions have been explored. Pristine Ni/CeO$_2$ is not stable as a result of coke deposition and surface reconstruction. In addition, co-feeding of H$_2$ can adversely influence the long-term stability of Ni/CeO$_2$. Ag severely reduces the intrinsic catalytic activity of Ni/CeO$_2$ catalyst, while enhances the long-term stability by diminishing coke deposition. Ag is applicable as a promoter under various reaction conditions, from N$_2$ diluted feedstock to H$_2$ co-fed and carrier-gas free feedstock. Kinetic studies show that Ag elevates the activation energy from 91 to *ca.* 140 kJ/mol by a loading of 0.3 mol.%, excessive Ag loading does not affect activation energy. The role of Ag is to block step sites on Ni surface that is associated with carbon nucleation and growth, and to promote gasification of coke formed. Besides, Ag alters the type of coke formed over Ni surface from recalcitrant whisker/encapsulating carbon to easily gasifiable amorphous carbonaceous species.

1. Introduction

Methane and carbon dioxide dry reforming (DRM, reaction (1)) has received renewed

$$CH_4 + CO_2 = 2H_2 + 2CO \quad \Delta H^o_{298} = +247 kJ/mol \tag{1}$$
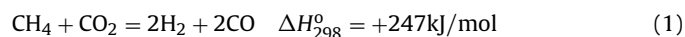
interest as a means to alleviate global warming by utilizing the two greenhouse gases to provide a useful feedstock of syngas (H$_2$/CO mixture) [1–4]. Besides, compared with commercial methane steam reforming (MSR) process that produces syngas with H$_2$/CO ratio of 3, DRM produces syngas with a lower H$_2$/CO ratio close to 1. Such a low ratio is more appealing to synthesis of downstream oxygenated chemicals such as acetic acid, dimethyl ether, oxo-alcohols, etc. [5]. In practical MSR process, an O/C ratio of above 3 is normally adopted to suppress the deposition of coke, while the MSR process suffers from an energy penalty, for heating excessive steam to *ca.* 800 °C [5]. The DRM process is suitable for converting field gas and biogas that contains large portion of CO$_2$ in addition to CH$_4$ directly into syngas without separation of CO$_2$. Combining with MSR, DRM can be adjusted into an economical route to convert methane into syngas with suitable H$_2$/CO ratio for methanol production, as recently proposed by Olah et al. [6]. Moreover, the strong endothermic nature of the reaction allows an energy transmission system to be designed based on it to store and convert nuclear or solar power [7–10]. DRM can be commercially viable when legislation requires reduction of CO$_2$ emission and its recycling becomes mandatory in the future.

Both noble metals (Ru, Rh, Pt, etc.) and group VIII (Fe, Co, Ni) metals are active in catalyzing DRM [1,7,8]. Despite the fact that noble metals are insensitive to coke formation, Ni is widely used in industry due to the high activity, wide-availability and low-price. The main technical issue arisen by Ni catalyst is the strong propensity to carbon deposition. Carbon deposition on Ni based catalysts can cause deactivation, pulverization of catalyst pellets, or large pressure drop. Reactions such as methane decomposition (reaction (2)), CO disproportionation (also known as Boudouard reaction) and CO reduction can contribute to

$$CH_4 = 2H_2 + C \quad \Delta H^o_{298} = 74.9 kJ/mol \tag{2}$$

$$2CO = CO_2 + C \quad \Delta H^o_{298} = -172.5 kJ/mol \tag{3}$$

$$CO + H_2 = H_2O + C \quad \Delta H^o_{298} = -131 kJ/mol \tag{4}$$
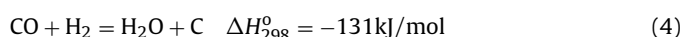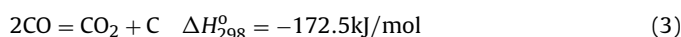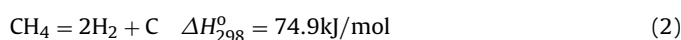
* Corresponding author. Tel.: +86 21 64253509; fax: +86 21 64253528.
E-mail address: kakezhu@ecust.edu.cn (K. Zhu).

coke deposition. DRM is normally performed at high temperatures (700–900 °C) to achieve high conversions for the endothermic nature of the reaction [11]. Carbon deposition is therefore mainly from methane decomposition that is thermodynamically favorable at reforming conditions. Wei and Iglesia [12] have disclosed that CH$_4$ deprotonation is the rate-determining step at high temperatures (823–1023 K) for both the DRM and decomposition reactions, so the kinetic law for the DRM can be expressed as: $r = kP^1_{CH_4}$.

This experimental measurement coincides with the theoretical reaction mechanism and related kinetics studies, which strongly advocate that methane deprotonation demands higher energetic barrier than further deprotonation of CH$_x$ ($x \leq 3$) [13,14]. Further deprotonation progressively accelerates as a consequence of lower activation barrier for deprotonation of CH$_x$, that is in line with the scaling rule for adsorption energies of CH$_x$ species with *C. In early studies, it is believed that carbon formation is associated with alkane dissociation into surface *C atoms, as *C dissolves into Ni particles, forming Ni$_3$C and subsequently precipitates at dislocation sites [15]. In spite of the fact that traces of Ni$_3$C have been indeed observed by in situ XRD studies [16], more and more experimental evidences and theoretical modeling results support that the formation of coke is mainly a surface phenomenon on Ni surface [13,14,17–22]. The face centered cubic (fcc) structure of Ni and low graphene-Ni lattice strain energetically favors surface chemisorption of *C, which is different from Fe that has a body centered cubic (bcc) structure and can form Fe$_3$C or Fe$_2$C$_5$ more facily, as recently unveiled by Saadi et al. [22] through theoretical modeling. Henceforth, carbon atoms can accumulate on Ni surfaces when carbon deposition rate is higher than the gasification rate, as proposed by Bengaard et al. [14]. High coverage of *C on Ni surface can induce the nucleation and growth of carbon, resulting in the formation of polymeric carbon, whisker carbon or encapsulating graphite carbon, depending on the reaction conditions and catalyst structures [13,14,17]. In situ TEM studies carried out by Helveg et al. [17] and theoretical simulations demonstrate that the nucleation and growth of carbon is structure sensitive and the surface structure of Ni particles are both dynamic and dependent on the gas constituents. The step sites on Ni surface are required for nucleation and growth of *C into whisker or encapsulating carbon, as the under-coordinated sites favors high *C coverage [13,14,17]. Further growth is mainly driven by the migration of *C from step sites to terraces on Ni surface. The larger the particle is, the more susceptible the Ni catalyst is towards carbon nucleation and growth [13,14,23,24].

Efforts to minimize carbon formation have a long history, several strategies have thus far been developed to circumvent carbon deposition upon Ni surface. The first successful strategy to inhibit coke deposition on Ni catalyst in MSR is the SPARG (sulphur-passivated reforming) process developed by Rostrup-Nielsen et al. [25] in Haldor Topsøe, whereby the under-coordinated sites on Ni surface are blocked by a small portion of H$_2$S in the feedstock. The gas phase H$_2$S is equilibrated with *S adsorbed at Ni surface. The partial pressure of H$_2$S is strictly controlled in order that only the carbon nucleation centers at the step sites are preferentially blocked [18,26]. The SPARG process still needs to separate the H$_2$S for downstream use of the syngas product, as H$_2$S can poison most catalysts. On the other hand, a series of metal promoters have been proposed to be effective in suppressing the coking of Ni surface. Among these metal promoters, Au can form surface alloy with Ni for the negative segregation energy ($\varepsilon_{segre} < 0$) and the positive mixing energy ($\varepsilon_{mix} > 0$) [27]. The incorporation of Au on Ni surface has been corroborated by scanning tunneling microscope (STM) measurements, and is found to enhance the long term stability for steam reforming of n-butane [28]. Similarly, Ag [29,30], Sn [31,32], Bi, As, Pb, etc. [15] also possess the coke-resistant properties in alkane reforming reactions. Meanwhile, the alkaline earth metal oxides, such as

MgO, CaO, SrO and BaO, are found to contribute to the reduction of coke deposition when used as supports or promoters [33–37]. The role of alkaline earth metal oxides is to form solid solution with NiO, thus the small particle size of metallic Ni after solid solution reduction can inhibit carbon deposition [3,11,12,24,35,36,38–41]. The metal-support interaction plays a key role in keeping the metallic particle size small under reducing and reforming conditions. The role of BaO in steam reforming of CH$_4$ is proposed to enhance the gasification of deposited coke at the Ni/BaO interface by Yang et al. [37]. Alkali metals, such as K, have been employed in practice as coke-resistant promoters, and the role of alkali metals is believed to reduce the CH$_4$ dissociation probability, as it incurs a decrease in prefactor of Arrhenius plot [14]. In addition, rare earth metal oxides are also employed as Ni supports in DRM, Ce-ZrO$_2$ [42], YSZ (Yttria-stabilized zirconia) [43] have exhibited stability in recent reports.

Ni supported CeO$_2$ has been utilized as catalysts in DRM, for CeO$_2$ is well-documented for the oxygen storage capacity (OSC), but whisker carbons have been found on pristine Ni/CeO$_2$ catalysts in reforming reactions [44–47]. It is thereby necessary to add promoters to enhance the robustness of the system. In previous studies, Nørskov et al. and Chorkendorff et al. [27,48] have theoretically predicted strong segregation energy of −0.58 eV for Ag in Ni, together with a large positive second derivative energy (0.99 eV), implying Ag resides on the surface of Ni particles. Vang et al. [29] have observed experimentally that Ag stays at the Ni surface by blocking the step sites preferentially, resulting in a lower C–C bond cleavage rate in ethylene hydrogenesis. Later, Parizotto et al. [30] have shown that Ag can effectively control the coke formation on Ni/Al$_2$O$_3$ for MSR, functioning in a way similar to that of Au. Similar results have been reported on Ag promoted Ni/YSZ for internal reforming in fuel cells, but slow deactivation over time-on-stream is also observed [43]. The promoting role of Ag in Ni/MgAl$_2$O$_4$ catalyst has also been explored by Jeong and Kang [49] for steam reforming of butane, and by Chorkendorff et al. [48] for the steaming of ethane. Recently, Zhu et al. [20,50] have carried out DFT calculations to understand the role of Ag in DRM, suggesting that Ag can be a promoter in inhibiting coke deposition. It is therefore desirable to explore the catalytic performance of Ag promoted Ni catalysts to understand the effects on reaction kinetics and types of carbon formed.

In this work, we explore the promoting role of Ag in Ni/CeO$_2$ catalyst for the DRM reaction, with the aim to enhance carbon tolerance and understanding the role of Ag. The catalytic performances of Ag promoted Ni/CeO$_2$ catalysts under different Ag contents are explored in DRM under carrier-gas diluted and carrier-gas free conditions, as well as H$_2$ co-feeding condition. The structure changes of the catalysts during preparation and after catalytic tests are characterized by combined techniques. The carbon content and types are determined to quantify the coke tolerance behavior. Kinetic studies are conducted for the pristine and Ag promoted samples to understand if Ag affects the active centers.

2. Experimental

2.1. Catalysts preparation

Nickel nitrate (≥98.5%) and anhydrous methanol (≥99.5%) were purchased from Sinopharm Chemical Reagent Co. Ltd. Cerium (III) acetate (≥ 99.99%) was provided by Shanghai Diyang Chemical Company. Benzyl alcohol (≥99.0%) was purchased from Shanghai Lingfeng Chemical Reagent Co. Ltd. Silver nitrate (≥99.8%) was purchased from Shanghai chemical Reagent Co. Ltd. All chemicals were used directly as provided. Ceria as a support was prepared

via solvothermal method developed by some of us [51]. Ni was introduced by impregnation of nickel nitrate solution with ceria and drying via rotary evaporation to achieve improved distribution of Ni. These samples have been calcined at 800 °C for 6 h via a ramp of 2 °C/min in the muffle oven. The high temperature calcination was necessary because the DRM was conducted at 760 °C, and normally higher temperatures were adopted in calcination step to avoid any thermal structure change during subsequent catalytic tests. Ag was introduced successively after nickel introduction in the same way, in order that Ag can be introduced onto the catalyst surface. The final products with 10 mol.% Ni as active sites and 0.3 mol.%, 0.6 mol.% and 2.4 mol.% Ag as promoter were denoted as Ni/CeO$_2$, Ni/CeO$_2$-3Ag, Ni/CeO$_2$-6Ag and Ni/CeO$_2$-24Ag, respectively. A CeO$_2$ sample synthesized by the recipe from [51] was calcined at 800 °C for 6 h for comparison in H$_2$-TPR measurements.

2.2. Characterization techniques

Powder X-ray diffraction (XRD) patterns were recorded on a Rigaku D/Max-RC powder diffractometer using Cu Kα radiation (operated at 40 kV and 100 mA, λ = 1.54178 Å). The diffractograms were collected in the 2θ range of 10–80° with a 2θ step size of 0.01° and a step time of 10 s.

TEM images of the samples were conducted on a JEM-2100 instrument operated at 200 kV. The samples were prepared via dispersing in ethanol on 400 mesh copper grids pre-coated with thin carbon films. Pretreatment under ultrasonication was used to disperse the powder before each measurement.

Specific surface areas were deduced from N$_2$ physisorption isotherm measurement using the standard Brunauer–Emmett–Teller (BET) model. Before measurements, all of the samples were subject to degassing at 350 °C overnight under vacuum to remove the surface contaminants.

H$_2$-temperature programmed reduction (H$_2$-TPR) was investigated by heating the samples in H$_2$ (5 vol.%)/Ar flow (30 mL/min) at a heating rate of 10 °C/min from 20 to 850 °C, and soaked at 850 °C for 30 min till no H$_2$ consumption was observed. The H$_2$ consumption was monitored by thermo-conductivity detector (TCD). For each measurement, 100 mg sample was placed at the bottom of the U-shaped quartz tube, which was pretreated at 120 °C under Ar atmosphere before the measurement.

X-ray photoelectron spectra (XPS) analyses were performed on a Thermo Fisher Scientific ESCALAB 250Xi spectrometer, using Al-Kα radiation (1486.6 eV, pass energy 20.0 eV) and recorded at θ = 90° of X-ray sources. The base pressure of the instrument was 1×10^{-8} to 1×10^{-9} Torr. The background contribution B (E) (obtained by Shirley method) caused by inelastic process was subtracted, whereas the curve-fitting was performed with Gaussian–Lorentzian profile by the standard XPS PEAK 4.1 software. The binding energies (BEs) over supported catalysts were calibrated using C 1s peak at 284.8 eV.

Thermogravimetric analysis (TGA) was performed on a thermogravimetric analyzer Pyris 1 TGA (purchased from Perkinelmer) under air to estimate the deposited coke amount of the spent catalysts. The samples were heated in air flow at a heating ramp of 10 °C/min to 800 °C, with the flow rate kept at 50 ml/min.

Temperature-programmed oxidation (TPO) was performed on a Quantachrome CHEMBET - 3000 instrument equipped with a thermal conductivity detector (TCD). For each measurement, ca. 50 mg of catalyst was loaded into a U-shaped quartz tube, mounted with quartz wool at both sides. The samples were pretreated in He flow at 300 °C for 1 h and then cooled down to 200 °C before measurement. After that, the gas mixture (5 vol.% O$_2$ in He) was fed into the tube with a total flow rate of 50 ml/min and the sample was then heated up to 800 °C with a ramp of 10 °C/min. The products were

also analyzed by an on-line mass spectrometer (AMETEK ProLine Mass Spectrometer).

2.3. Catalytic assessments

The assessments of the catalytic performance were conducted in a fixed-bed reactor made of quartz tube (ϕ 14 mm × 2 mm) at 560–760 °C under atmospheric pressure. After calcinations, 300 mg catalyst was pressed into pellets and sieved to 40–60 mesh. The catalyst bed was diluted with quartz sand of the same size and mounted into the tubular reactor with quartz wool. The mounted catalyst was in situ reduced by hi-purity H$_2$ (60 ml/min, 800 °C) for 2 h prior to catalytic reaction. All the gas cylinders were purchased from Shanghai Dumao Air purified gas Co. Ltd., with the purity of 99.999% for H$_2$, CH$_4$, N$_2$ and 99.995% for CO$_2$, respectively. The feed gas flow rate to the reactor was set at 68 ml/min (GHSV$\approx$13, 400 ml h^{-1} g^{-1}-cat), with a molar ratio of CH$_4$:CO$_2$:N$_2$ = 25:25:18 under normal reaction condition. A harsh condition was also adopted with carrier-gas N$_2$ free (CH$_4$:CO$_2$ = 25:25) under otherwise identical conditions. In the catalytic tests with co-fed H$_2$, 1 vol.% H$_2$ was charged into the feed gas to explore the effect on catalytic performances under reducing atmosphere, analogous to the industrial practice.

The effluent gas was analyzed by GC-9860 (Shanghai Qi Yang Instrument), equipped with a TDX-01 column and an on-line TCD. CH$_4$, CO$_2$ conversions, selectivity to H$_2$ and CO, H$_2$/CO ratio are defined as follows:

$$X_{CH_4} = \frac{F_{CH_4,in} - F_{CH_4,out}}{F_{CH_4,in}}, \quad X_{CO_2} = \frac{F_{CO_2,in} - F_{CO_2,out}}{F_{CO_2,in}},$$

$$S_{H_2} = \frac{F_{H_2,out}}{(F_{CH_4,in} - F_{CH_4,out}) + (F_{CO_2,in} - F_{CO_2,out})},$$

$$S_{CO} = \frac{F_{CO,out}}{(F_{CH_4,in} - F_{CH_4,out}) + (F_{CO_2,in} - F_{CO_2,out})},$$

$$H_2/CO = \frac{S_{H_2}}{S_{CO}}.$$

To understand the effect of Ag over activation energies, the kinetic experiments were carried out under the same conditions adopted previously by us [40]. For each measurement, only 70 mg catalyst (40–60 mesh) was pressed into pellets and sieved to 40–60 mesh, mounted into the reactor and reduced in H$_2$ for 2 h. Reaction rates were measured at low methane conversions (below 5%) to avoid the effect of reverse reaction. In addition, the catalyst was diluted by γ-Al$_2$O$_3$ powders, followed by mixture with 500 mg quart S$_{BET}$ sand of the same size, to ensure isothermal operations. Based on literature and our previous tests [40], mass transfer was mostly eliminated under such operating conditions of high flow rate and small catalyst particle sizes [12,52]. Appropriate criteria were employed to ensure the validity of these measurements. From previous reports, it has been confirmed that the reaction rate of methane reforming is first order of P_{CH_4} and can be expressed as $r = kP_{CH_4}^1$ [12,13], from which can the activation energy be derived.

3. Results and discussion

3.1. Characterization of fresh catalysts

The XRD patterns (Fig. S1, Supporting Information) show that the principal phase of the fresh catalysts after calcination is fluorite structured CeO$_2$ (JCPDS No. 34 - 0394), while most of NiO is dissolved in CeO$_2$ as only three small blunt peaks ($2\theta \approx$ 37.25°, 43.28°, 62.88°) attributable to (1 1 1), (2 0 0) and (2 2 0) reflections from rocksalt structured NiO (JCPDS No.78 - 0643, space group: Fm-3m). Rodriguez and co-workers [47,53] have demonstrated that NiO can dissolve in fluorite CeO$_2$ structure with a solubility close

Table 1
Surface areas of fresh catalysts and coke deposition amount of spent catalysts.

Catalysts	(m^2/g)	Coke content[a] (%)		
		100 h normal condition	100 h H_2 co-feed normal condition	100 h harsh condition
Ni/CeO$_2$	13.6	3.189	2.917	7.24
Ni/CeO$_2$-3Ag	9.8	0.251	0.035	2.23
Ni/CeO$_2$-6Ag	14.1	0.961	1.199	0.9
Ni/CeO$_2$-24Ag	10.9	0.097	n.d.	0.73

[a] Measured by TGA.

to 10–12 mol.%, which is limited mainly because each Ni^{2+} in NiO rocksalt structure is surrounded by 6 O^{2-}, whereas in the fluorite structure by 8. Herein, in our preparation the NiO content is 10 mol.%, but still traces of NiO are detectable. We ascribe the difference to the effect of preparation history, as Rodriguez et al. [53] have adopted a reverse-microemulsion protocol for their synthesis and the calcination temperature is 500 °C. A calculation from Bragg's law gives the lattice constant of 5.4110 Å for Ni/CeO$_2$, which is close to the reference value of 5.4134 Å for CeO$_2$ (JCPDS No. 34 - 0394). This observation together with the weak NiO diffraction strongly manifests that most Ni^{2+} is incorporated into the fluorite structure. In general, Ce–Ni exchange within CeO$_2$ should lead to an obvious contraction of lattice parameter. Herein as the formal charge on Ni^{2+} is much smaller than Ce^{4+}/Ce^{3+}, vacancies must be introduced into the mixed-metal oxide. The creation of oxygen vacancies causes lattice expansion that compensates the lattice contraction by Ni–Ce exchange, resulting in a lattice close to pristine CeO$_2$ [53]. When Ag is introduced on Ni/CeO$_2$ catalyst at loadings below 0.6 mol.% Ag, no additional diffractions can be identified. For the Ni/CeO$_2$-24Ag, one weak peak at $2\theta = 38.116°$ ascribable to (1 1 1) diffraction from Ag-3c phase (JCPDS No. 04 - 0783) can be noticed, as shown in Fig. S1d, and inset. This observation is similar to previous observations for Ag/CeO$_2$, for which no Ag or Ag$_2$O diffraction peaks are distinguishable when the loading is low, but for higher loadings Ag diffraction is observable [54]. The variation in BET surface areas is small with loading of Ag, as listed in Table 1. Elemental mapping results of three typical samples, i.e., Ni/CeO$_2$-3Ag, Ni/CeO$_2$-6Ag and Ni/CeO$_2$-24Ag, are manifested in Fig. S2. All elements are uniformly distributed for the calcined Ni/CeO$_2$-3Ag and Ni/CeO$_2$-6Ag samples, but Ag zoning has been found for Ni/CeO$_2$-24Ag, that is in line with XRD results.

H$_2$-TPR has been employed to investigate the influence of Ag to the reducibility of Ni^{2+} and Ce^{4+} ions in these catalysts, the results are illustrated in Fig. 1. For the reference CeO$_2$, there is only one envelope centered at 811 °C, ranging from 650 to 900 °C, can be found, which is attributed to the reduction of inner most

lattice oxygen of CeO$_2$ [51,54]. The profile differs from what we observed before for the sample calcined at 400 °C, which is rich in surface oxygen species [51], because the high calcination temperature (800 °C) has annihilated the Ce^{3+} species that is associated with easily reducible surface oxygen moieties. One low temperature reduction envelope with onset temperature at 310 °C and centered at *ca.* 434 °C arising from reduction of extra framework NiO is seen [45,53], indicating that some of NiO presents as supported NiO, which is also confirmative to the XRD observations. The reduction of NiO phase is completed at temperatures below 600 °C, which is also in agreement with previous TPR measurements [45,55]. Rodriguez et al. [53] have observed the reduction of Ni^{2+} cations embedded in the ceria lattice from 400 to 700 °C for a Ni$_{0.1}$Ce$_{0.9}$O$_{2-y}$ sample derived from microemulsion protocol. Therefore, the contribution from Ni^{2+} dissolved in CeO$_2$ solid solution can be included in the reduction process. The reduction of lattice oxygen centered at 859 °C is seen to shift towards higher temperatures with respect to the reference CeO$_2$ sample, showing that the Ni–O–Ce bond in the mixed oxide is stronger than the Ni–O in NiO or the Ce–O bond in CeO$_2$. Besides, small reduction peaks below 290 °C associated with reduction of surface Ni^{3+} reduction can also be identified for Ni/CeO$_2$ [56]. When Ag is introduced to Ni/CeO$_2$, systematic shift of reduction peaks can be found hand-in-hand with the increase of Ag loading, for both the low temperate and high temperature reduction envelopes, whereas the shift is more prominent for the low temperature ones. When Ag loading increases from 0, 0.3 to 0.6 mol.%, the low temperature reduction peak decreases from 434 to 387 and 320 °C, respectively. Ag incorporation into CeO$_2$ normally weakens the Ce–O bonds and lowers the reduction temperature accordingly [54], hence the phenomenon shows that Ag has close contact with Ni/CeO$_2$ at the interfaces. The Ni/CeO$_2$-24Ag sample has the same low reduction temperature as Ni/CeO$_2$-6Ag, at 320 °C, hinting that Ag has saturated the surface of Ni/CeO$_2$. The high temperature reduction peaks for Ni/CeO$_2$, Ni/CeO$_2$-3Ag, Ni/CeO$_2$-6Ag and Ni/CeO$_2$-24Ag appear at 859, 838, 833 and 804 °C, respectively. At low loadings, for Ni/CeO$_2$-3Ag and Ni/CeO$_2$-6Ag, the shift is small, but becomes obvious when crystalline Ag presents for Ni/CeO$_2$-24Ag. The fact that there is no separate reduction peaks found in the H$_2$-TPR patterns also implies that the oxygen on the catalysts are highly mobile, and can spill facilely on the catalyst surface. It is also important to note that previous in situ studies carried out by Caballero et al. [45] using XANES have demonstrated that the behavior of Ni^0 particles in Ni/CeO$_2$ catalyst under reducing H$_2$ atmosphere is similar to that observed under DRM reaction conditions. Therefore, this information is helpful to understand the structure/composition under reaction relevant conditions.

The XRD patterns of the reduced samples (shown in Fig. S3) after pretreatment in H$_2$ have exhibited no obvious shift of lattice parameters with respect to the unreduced fluorite structure, indicating that the fluorite main phase is robust towards reduction. A $a = 5.4114$ Å can be derived from the XRD data for Ni/CeO$_2$ with fluorite structure, and other samples have close values. Previously studies by in situ techniques (XRD/XANES/EXAFS) [53] have shown that it is less likely to reduce all the NiO in the fluorite
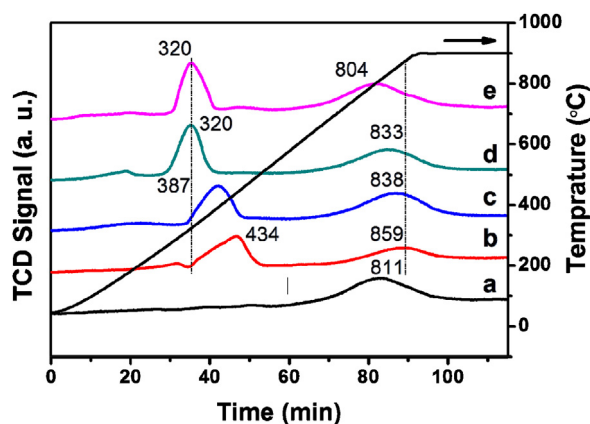

Fig. 1. H$_2$-TPR profiles for fresh catalysts CeO$_2$ (a), Ni/CeO$_2$ (b), Ni/CeO$_2$-3Ag (c), Ni/CeO$_2$-6Ag (d), Ni/CeO$_2$-24Ag (e).

lattice, as some NiO interacts strongly with the lattice in the fluorite $Ni_xCe_{1-x}O_{2-y}$ solid solution. Meanwhile, diffraction peak at $2\theta \approx 44.507°$ owing to the (1 1 1) diffraction that possesses the highest intensity ($I_{(1\ 1\ 1)} = 100$) for reduced metallic Ni^0 (JCPDS No. 04 - 0850) can be discerned, showing that the Ni/CeO_2 has been partially reduced. For Ni/CeO_2-24Ag, a diffraction peak from metallic Ag^0 (JCPDS No. 04 - 0783) can also be identified, but is absent for samples with lower Ag loadings. From the XRD results, it is plain that NiO has been reduced into metallic Ni^0 during H_2-TPR or in situ reduction.

3.2. Catalytic tests under normal condition

3.2.1. The catalytic activity versus temperature tests

The catalysts mounted into the tubular reactor have been reduced in situ at 800 °C for 2 h before catalytic evaluations. We set a normal reaction condition to take a first-step watch on the performances of the catalysts. In the first series of exploration, the activities of the catalysts are tested at temperatures from 560C to 760 °C with an interval of 50 °C. To slow down the possible deactivation during the tests, a diluent N_2 has been co-fed. Fig. 2 displays the activity versus temperature plots, a thermodynamically feasible conversion is observed at approximately 560 °C [11] for the pristine Ni/CeO_2. The conversions of both CH_4 and CO_2 increases with temperature as expected. The H_2/CO is also dependent on CH_4 conversion, because the reaction is escorted by simultaneous reverse-water-gas-shift (RWGS) reaction:

$$CO_2 + H_2 = H_2O + CO \quad \Delta H^o_{298} = -41.1 kJ/mol \quad (5)$$
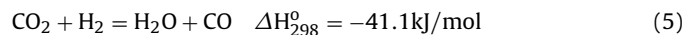
The RWGS affects the H_2/CO because the reaction rate is faster than DRM on Ni surfaces [12]. At 560 °C, the CH_4 conversion of 10.67% is observed for Ni/CeO_2, but only 1.52% for Ni/CeO_2-3Ag is detected, suggesting that Ag significantly reduces the conversion of CH_4 on Ni surfaces. As a rule, the activity decreases with the increase of Ag loading for all the temperatures range assessed. The passivation effect is pronounced from Ni/CeO_2 to Ni/CeO_2-3Ag, with CH_4 conversion dropped from 82.15% to 19.14% at 760 °C. Further increase of Ag loading induces less prominent reduction in activity, and CH_4 conversions of 14.51% and 13.29% are found for Ni/CeO_2-6Ag and Ni/CeO_2-24Ag, respectively. The same trend is also seen for CO_2 conversions throughout the tests. These results show that Ag has effectively lowered the intrinsic activity of Ni surfaces, and the effect is either at the surface or electronic.

There are two types of active sites over Ni surfaces, e.g., the terrace sites and under- coordinated sites (represented by step sites in theoretical modelling). For pristine Ni surfaces, the predominate activity derives from the step sites for the low activation energy and corresponding high reaction rate, despite the fact that there are more terrace sites than step sites [14,28]. Ag and Ni have a strong energetic driving force to form surface alloy rather than bulk alloy, whereby Ag locates on the step sites [26,29]. The blockage of these reactive step sites on Ni surfaces shifts the active centers for methane activation from step sites to less reactive terrace sites, consequently, there is an obvious passivation observable for Ag–Ni system [26,29]. Similar results have been observed by some previous reports [30,43,48]. Besides, the presence of Ag on Ni surfaces can also passivate the neighboring Ni atoms, as suggested by some recent theoretical modeling results [20]. The reaction is accompanied by the RWGS reaction, and reaction rate determination has shown that the rate for RWGS is higher than methane deprotonation [12]. Consequently, the fast RWGS reaches equilibrium quickly. For the Ag-promoted catalysts, the conversion of methane and CO_2 are lower as a result of surface passivation, more CO_2 and H_2 are converted into water and CO, which changes the product distribution.
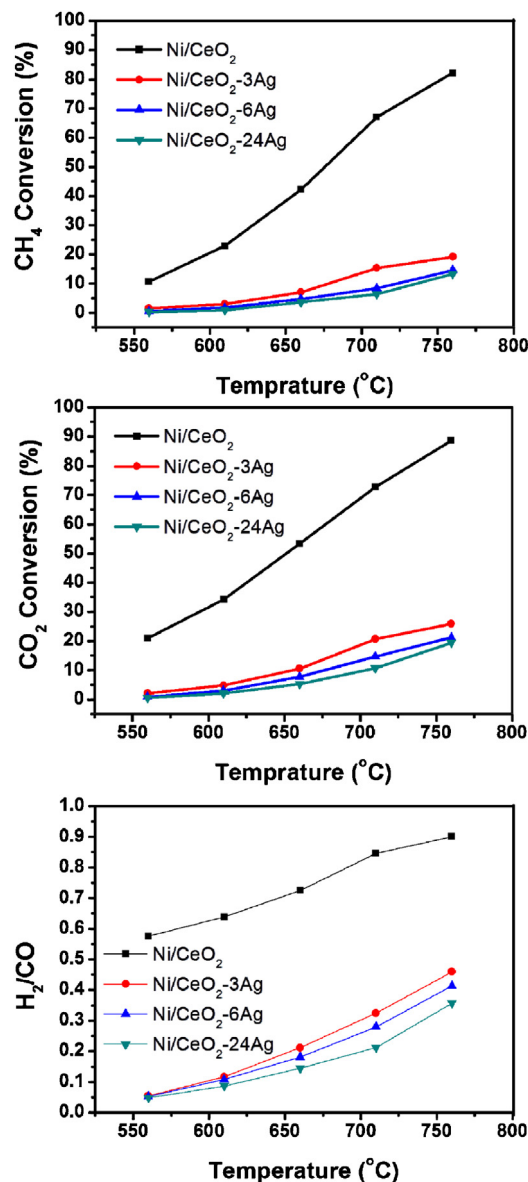

Fig. 2. The catalytic activity for CH_4 (a) and CO_2 (b) conversion as a function of temperature, together with the corresponding H_2/CO ratio (c).

3.2.2. The 100 h time-on-stream test with diluents N_2 gas

Afterwards, a series of 100 h time-on-stream catalytic tests have been conducted at 760 °C to show time-on-stream stability under the effect of Ag, as delineated in Fig. 3. Ni/CeO_2 manifests the highest initial activity ($X_{CH_4}\% = 81.85\%$), but a gradual deactivation has been found, only 65.18% is left after the 100 h test, as compiled in Table 2. With the increase of Ag content, the activity decreases, initial methane conversions are 24.92%, 14.15% and 12.87% for Ni/CeO_2-3Ag, Ni/CeO_2-6Ag and Ni/CeO_2-24Ag, respectively. The corresponding activities decrease to 20.96%, 12.76% and 11.76% after 100 h time-on-stream tests for the respective catalysts. The overall passivation trend is consistent with the results of relevant works reported before [43,57]. From these tests, one can conclude that Ag strongly suppresses the Ni surfaces, simultaneously enhances the catalytic durability in a diluted feedstock. When irreducible Al_2O_3 is used to support Ag-modified Ni catalyst for MSR, no obvious deactivation has been evidenced during time-on-stream test of 6 h [30], we therefore ascribe the small deactivation of Ag promoted catalysts to the effect of reducible CeO_2 support [45,58]. Slow deactivation of Ag promoted Ni/YSZ has also been
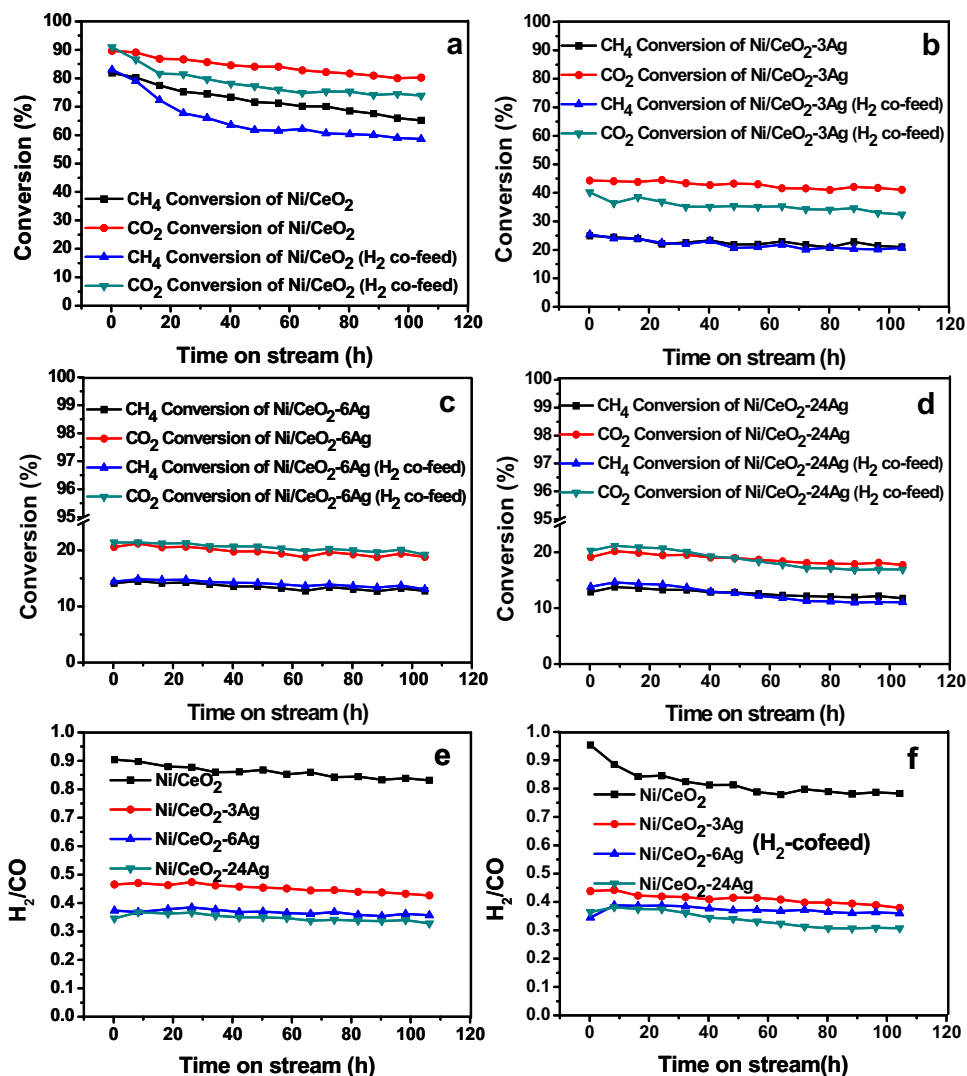
Fig. 3. Stability performance of the catalysts in 100 h time-on-stream tests with as N_2 diluent carrier-gas, in the absence and presence of co-feeding H_2, (a)Ni/CeO$_2$, (b)Ni/CeO$_2$-3Ag, (c) Ni/CeO$_2$-6Ag, (d)Ni/CeO$_2$-24Ag. The H_2/CO ratios are exhibited in (e) and (f) for the H_2 absence and presence tests, respectively.

observed by Neophytides et al. for internal CH_4 steam reforming in fuel cell [43], possibly due to the fact that YSZ is also a reducible support.

3.2.3. Catalytic performance tests when H_2 is co-fed

The catalytic performance under H_2 co-fed is important for several reasons. The Ni/CeO$_2$ system is a catalyst whose surface undergoes reconstruction with respect to adjacent gas component change, especially H_2 brings the reduction of support CeO$_2$ and the migration of CeO$_2$ to bury Ni surfaces [45,53,58]. The reducing atmosphere is found not only to influence the Ni–CeO$_2$ interaction, but also can be a crucial factor to determine the Ag–CeO$_2$

interaction strength [59]. Despite the fact that H_2 is a main product of DRM, the space velocity for the reaction is rather high (GHSV $\approx$ 13,400 ml h^{-1} g^{-1}-cat), which means that the upstream of the catalyst bed is not experiencing a reducing atmosphere than that at the downstream of the catalyst bed. In practical industrial use of Ni catalyst for MSR, normally, H_2 is co-fed to keep the Ni in its metallic state. From a reactor design angle, the H_2 co-feeding test gives the information of a more representative performance of the catalyst in the middle part of the reactor. In addition, such tests can provide the information on "what if the fluctuation in reactor causes a more reducing contacting atmosphere by deviating from nominal composition?"

Table 2
Catalysts for Ag promoted Ni-CeO$_2$ under different feeding conditions.

Catalyst	CH_4 conversion (%) under different feeding conditions					
	N_2 diluted		H_2-cofeeding		Diluent gas free	
	Initial activity	Final activity	Initial activity	Final activity	Initial activity	Final activity
Ni/CeO$_2$	81.85	65.18	82.98	58.63	82.82	67.05
Ni/CeO$_2$-3Ag	24.92	20.96	25.42	20.70	29.47	23.09
Ni/CeO$_2$-6Ag	14.15	12.76	14.39	13.08	28.28	23.04
Ni/CeO$_2$-24Ag	12.87	11.76	13.82	11.05	22.96	18.37

As shown also in Fig. 3, Ni/CeO$_2$ has an almost identical initial activity for H$_2$ co-feeding test, with X_{CH_4}% of 82.95% is detected. But the pristine catalyst deactivates at a faster rate than that tested without H$_2$, and a conversion of 58.63% is left by the end of 100 h time-on-stream (Fig. 3a). The same trend in terms of X_{CO_2}% can also be seen. It is thereby concluded that the pristine Ni/CeO$_2$ catalyst deactivates more quickly in the presence of small amount of H$_2$. These effects result from reduction of support CeO$_2$ to CeO$_{2-x}$, and the migration of reduced CeO$_{2-x}$ to bury Ni^0 surface, which will be elaborated in Section 3.6. For Ni/CeO$_2$-3Ag, the initial activity is found to be 25.42% for X_{CH_4}%, and deactivates to 20.70% after 100 h (Fig. 5b). X_{CO_2}% is affected due to the influence of RWGS, as H$_2$ co-feeding can convert more CO$_2$ into H$_2$O and CO, resulting in a lower CO$_2$ conversion. But Ni/CeO$_2$-3Ag performs as stable as that in the absence of H$_2$. Ni/CeO$_2$-6Ag and Ni/CeO$_2$-24Ag are unaffected by H$_2$ co-feeding, as manifested by the almost superimposable time-on-stream activity results shown in Fig. 3c and d. The H$_2$/CO ratio is quite similar for the H$_2$ co-feeding test and the test in the absence of H$_2$, as shown in Fig. 3e and f.

3.2.4. Catalytic tests under diluent-gas free conditions

To explore the effect of diluents gas over long term catalytic performances, a stoichiometric feed has been adopted under carrier-gas free conditions. Our previous tests have shown that when stoichiometric feed is employed without carrier-gas, the deactivation will accelerate, consequently, the stability difference widens [39]. As shown in Fig. 4, for the pristine Ni/CeO$_2$ catalyst, a continuous and slow deactivation is observed, and the deactivation in the initial 24.3 h is more prominent than during the rest of the time. An initial X_{CH_4}% of 82.82% is observed, which drops to 73.21% after 24.3 h, and at the end of 100 h test, a conversion of 67.05% can be inferred. For Ni/CeO$_2$-3Ag, Ni/CeO$_2$-6Ag and Ni/CeO$_2$-24Ag, the initial X_{CH_4}% are 29.47%, 28.28% and 22.96%, respectively, showing that Ag content increase brings about the reduction in Ni activity. The trend resembles that observed in the presence of N$_2$ diluted. By the end of the evaluation, the corresponding X_{CH_4}% dropped to 23.09%, 23.04% and 18.37% for Ni/CeO$_2$-3Ag, Ni/CeO$_2$-6Ag and NiCeO$_2$-24Ag, respectively. The curves of activities change with time-on-stream are almost identical for Ni/CeO$_2$-3Ag and Ni/CeO$_2$-6Ag, showing they have the same activity despite the difference in Ag loading. For Ni/CeO$_2$-24Ag, further passivation is seen, but not so obvious as from Ni/CeO$_2$ to Ni/CeO$_2$-3Ag. These explorations underline the promoting role of Ag to enhance the stability under harsh stoichiometric feeding conditions, when deactivation becomes fast. Still, a perceivable slow deactivation is seen even for Ag promoted catalysts, we tentatively attribute it to the effect of support that undergoes reconstruction.

3.3. Characterizations of spent catalysts under normal condition

The catalysts after 100 h reaction are characterized by combined XRD, XPS and TEM to determine the structural/composition variation. Fig. S4 illustrates the XRD patterns for spent catalysts tested under diluent gas feeding conditions, which are identical to those of the corresponding reduced samples (Fig. S3). For Ni/CeO$_2$ catalyst, a = 5.4108 Å can be inferred from the indexation for fluorite structure, only negligible shrinkage is seen. The same trend can be observed for the other Ag promoted catalysts. Therefore, even after a 100 h catalytic reaction, the integrity of the Ni/CeO$_2$ structure is still retained. Absence of graphitic carbon diffraction implies that the carbon deposition is either too low or non-graphitic in nature.

Three representative spent catalysts, Ni/CeO$_2$, Ni/CeO$_2$-3Ag and Ni/CeO$_2$-24Ag employed in the normal conditions have been subjected to XPS measurement to determine the chemical states and surface compositions, with the results summarized in Table 3, Table S1 (Supporting information) and Figs. 5–8. As XPS is a surface
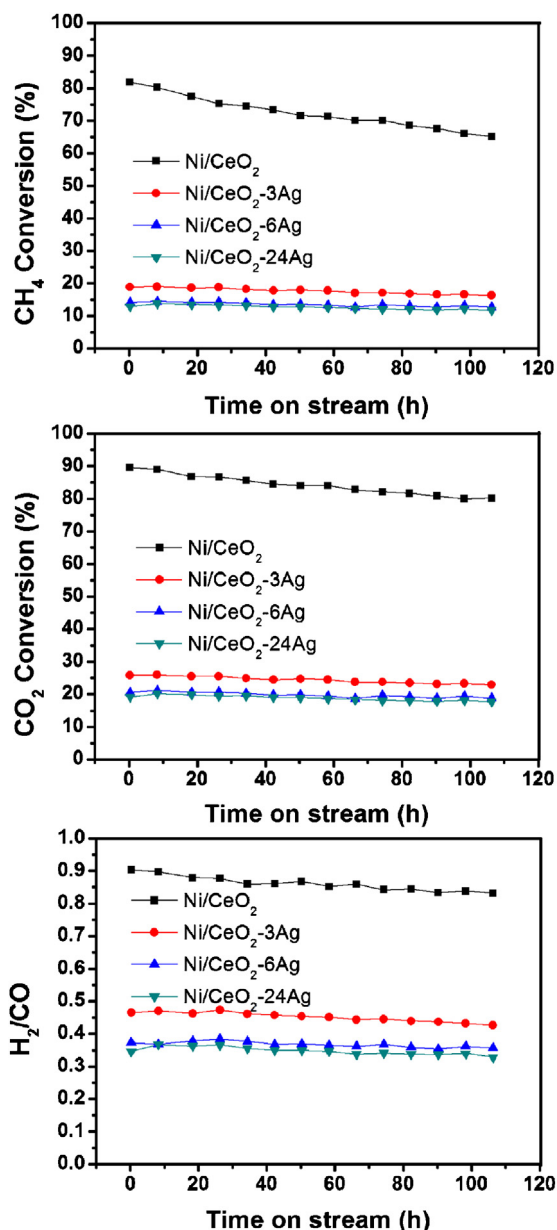

Fig. 4. Catalytic activity for CH$_4$ (a) and CO$_2$ (b) conversion as a function of time-on-stream in 100 h diluents-gas free tests, together with the corresponding H$_2$/CO ratio (c).

sensitive technique, it provides the composition at the catalyst surface. From Table S1, it is plain that when Ag content increases in the catalysts, the coke content decreases accordingly. The Ni content (21.6 mol.% and 28.4 mol.% on a metallic basis, for H$_2$ free and H$_2$ co-feeding tests, respectively) at the surface for Ni/CeO$_2$ is found to be higher than that in the bulk (10 mol.%), indicating a surface enrichment of Ni. For Ni/CeO$_2$-3Ag and Ni/CeO$_2$-24Ag, the surface contents for Ni are still above that of the bulk, showing Ag does not affect the Ni content enrichment at the catalyst surface. Interestingly, the Ag contents (1.14 mol.% and 1.00 mol.% metallic basis, for H$_2$ free and H$_2$ co-feeding tests, respectively) for the two samples appear close to the bulk (2.90 mol.%) for Ni/CeO$_2$-3Ag, which are lower than that for Ni/CeO$_2$-24Ag. Normally, as Ag and Ni forms surface alloy at the Ni surface, the Ag content should be higher than that in the bulk in XPS measurement. Indeed, Au and Sn that form surface alloys with Ni, respectively, whose concentrations have been found to be higher at the surface than that in the bulk
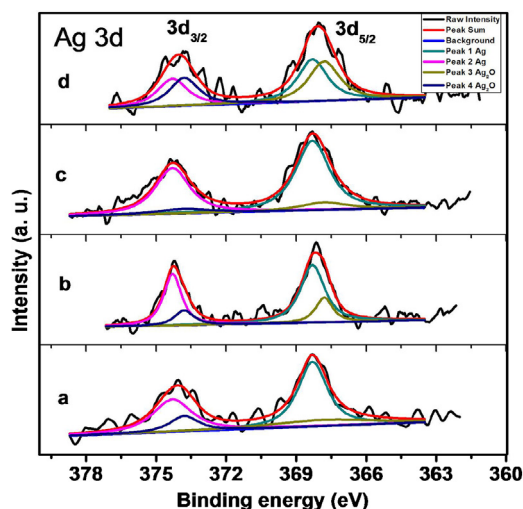
Table 3
Assignments of the fitting components for C1s, Ag 3d, Ni2p$_{3/2}$ and Ce 3d in XPS spectra of spent catalysts.

Catalysts	C 1s	Content	Ag 3d	Content	Ni 2p$_{3/2}$	Content	Ce 3d	Content
Ni/CeO$_2$	Ni$_3$C	0.00%			Ni^0	27.26%	Ce^{4+}	83.45%
	Graphite	83.03%			Ni^{2+}	72.74%	Ce^{3+}	16.55%
	CO$_3^{2-}$	16.97%						
Ni/CeO$_2$ (H$_2$ co-feed)	Ni$_3$C	0.00%			Ni^0	24.23%	Ce^{4+}	83.89%
	Graphite	80.92%			Ni^{2+}	75.77%	Ce^{3+}	16.11%
	CO$_3^{2-}$	19.08%						
Ni/CeO$_2$-3Ag	Ni$_3$C	0.63%	Ag	74.05%	Ni^0	21.98%	Ce^{4+}	74.35%
	Graphite	90.81%	Ag$_n^+$	25.95%	Ni^{2+}	78.02%	Ce^{3+}	25.65%
	CO$_3^{2-}$	8.56%						
Ni/CeO$_2$-3Ag (H$_2$ co-feed)	Ni$_3$C	0.35%	Ag	76.61%	Ni^0	19.19%	Ce^{4+}	83.45%
	Graphite	90.88%	Ag$_n^+$	23.39%	Ni^{2+}	80.81%	Ce^{3+}	16.55%
	CO$_3^{2-}$	8.77%						
Ni/CeO$_2$-24Ag	Ni$_3$C	7.93%	Ag	86.63%	Ni^0	6.40%	Ce^{4+}	59.44%
	Graphite	65.89%	Ag$_n^+$	13.37%	Ni^{2+}	93.60%	Ce^{3+}	40.56%
	CO$_3^{2-}$	26.17%						
Ni/CeO$_2$-24Ag (H$_2$ co-feed)	Ni$_3$C	17.28%	Ag	45.02%	Ni^0	8.03%	Ce^{4+}	69.41%
	Graphite	60.06%	Ag$_n^+$	54.98%	Ni^{2+}	91.97%	Ce^{3+}	30.59%
	CO$_3^{2-}$	22.66%						

[28,31,32]. The discrepancy can be understood by taking into the fact that partially reduced CeO$_{2-x}$ can migrate onto Ni surface and bury Ni particles into the support [45,53,58]. Similar situation can occur to the as formed Ag–Ni surface alloy.

In order to determine the chemical environment and oxidation states for Ni, Ce and Ag, XPS has been employed for the representative samples. Fig. 5 depicts the Ni 2p$_{3/2}$ patterns for the spent catalysts, together with the deconvolution of the envelopes. The major peak at 855.5–856.5 eV is attributed to the presence of Ni^{2+}

[60], while a satellite peak at *ca.* 861 eV can also be distinguished. Peaks centered at 852.7 eV are from Ni^0, which constitute only a small portion of the envelope, because contact of the spent catalyst with moisture or air can induce oxidation of the outermost layer of Ni [61,62]. The carbon species coverage on the Ni surface can also account for the low Ni^0 surface concentration (Table S1). Some

Fig. 5. Ni 2p$_{3/2}$ XPS patterns of spent catalysts tested under normal condition. (a)Ni/CeO$_2$, (b) Ni/CeO$_2$ (H$_2$ co-feed), (c)Ni/CeO$_2$-3Ag, (d) Ni/CeO$_2$-3Ag (H$_2$ co-feed), (e) Ni/CeO$_2$-24Ag, (f) Ni/CeO$_2$-24Ag (H$_2$ co-feed).

Fig. 6. Ce 3d XPS patterns of spent catalysts tested under normal condition. (a)Ni/CeO$_2$, (b) Ni/CeO$_2$ (H$_2$ co-feed), (c)Ni/CeO$_2$-3Ag, (d) Ni/CeO$_2$-3Ag (H$_2$ co-feed), (e) Ni/CeO$_2$-24Ag, (f) Ni/CeO$_2$-24Ag (H$_2$ co-feed).

Fig. 7. Ag 3d XPS patterns of spent catalysts tested under normal condition. (a)Ni/CeO$_2$-3Ag, (b) Ni/CeO$_2$-3Ag (H$_2$ co-feed), (c) Ni/CeO$_2$-24Ag, (d) Ni/CeO$_2$-24Ag (H$_2$ co-feed).

Ni^0 is also detected when the catalysts are exposed to the open, as the carbonaceous coverage prevents the Ni^0 surface from being oxidized. For Ni/CeO$_2$-24Ag, far less Ni^0 is determined, presumably due to the low coke content and the high likelihood of being oxidized in post-catalytic handling. By comparing the Ni 2p$_{3/2}$ patterns for Ni/CeO$_2$ with the Ag promoted samples, no new peaks can account for the Ag–Ni interaction. This observation is consistent with that made by Prieto et al. [63] for Ag–Ni bimetallic nanoparticles, as Ag–Ni interaction does not cause substantial chemical shift. From Table 3 and Fig. 6, both Ce^{3+} and Ce^{4+} are found to co-exist in the spent samples. Ce^{3+} content is proportional to oxygen vacancies [64], reflecting the reduction degree of support during the course of the catalytic tests. Ag loading increases hand-in-hand with the amount of Ce^{3+} on Ni/CeO$_2$ for the spent catalysts (Table 3). From the XPS spectra of Ag 3d shown in Fig. 7, the peak with a chemical shift of 368.4 eV is assigned to Ag^0 interacting with CeO$_2$ [65], and the 367.8 eV peak is associated with positively charged Ag$_n^+$ cluster, when charge transfer occurs between Ag cluster and support CeO$_2$ [54]. Prieto et al. [63] have assigned the shift towards lower binding energies in bimetallic Ag-Ni alloy to the existence of Ag$^+$. The previous theoretical estimation and experimental measurements of Ag–Ni and Ag–CeO$_2$ interaction are inconsistent with each other, and are dependent upon contacting atmosphere [20,48,59].
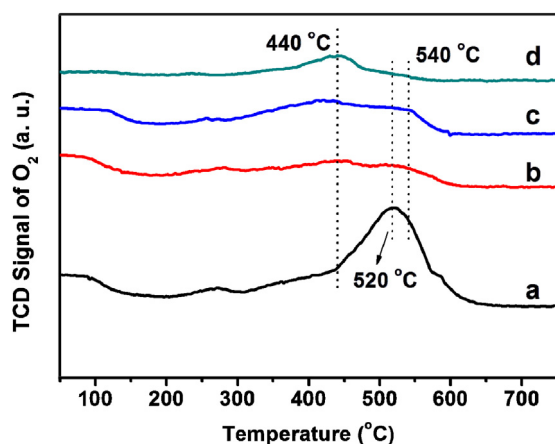

Fig. 8. O$_2$-TPO patterns of spent catalysts tested under normal condition, Ni/CeO$_2$ (a), Ni/CeO$_2$-3Ag (b), Ni/CeO$_2$-6Ag (c), and Ni/CeO$_2$-24Ag (d).

Therefore, whether Ag$^+$ or Ag$_n^+$ cluster exists cannot be decided by XPS of Ag 3d alone. The increase of Ce^{3+} content with Ag loading suggests that Ag$_n^+$ is more likely to be the positively charged Ag species that balances the negative charge of surface vacancies [54]. This assignment is also supported by the fact that the chemical shift is very small when Ag alloys with other metals [66,67]. The contribution from Ag–Ni alloy can appear at close to 368.4 eV, which is indistinguishable from mono-metallic Ag. Although stoichiometric compounds Ag$_2$O and AgO tend to decompose at temperatures above 230 and 100 °C, respectively, the metallic Ag is permeable to oxygen that dissolves into the metal at high temperatures [68]. Such dissolution can lead to the oxidation of Ag and formation of Ag$^+$ or Ag$_n^+$ cluster. For Ni/CeO$_2$-3Ag, the ratio Ag/Ag$_n^+$ does not vary with co-fed H$_2$, as only surface Ag species present. In contrast, for Ni/CeO$_2$-24Ag, where crystalline Ag clusters exist (Fig. 7, Table 3), the co-fed H$_2$ has promoted the content of Ag$_n^+$ (from 43.16% to 54.98%) that interacts strongly with reduced CeO$_{2-x}$ support. This deduction is in line with the measurement carried out by Campbell et al. [59], who have found that reduced CeO$_{2-x}$ interacts more strongly with Ag.

TG, XPS, O$_2$-TPO as well as TEM have been employed to determine the formed carbon to understand the effect of Ag on the amount and types of carbon deposition on the spent catalysts. The TG results exhibited in Table 1 clearly show that the addition of Ag can reduce the amount of coke deposition, and 0.3 mol.% Ag is enough to substantially reduce the amount of coke formation. The surface composition results are listed in Table S1, where less coke is found on Ag promoted catalysts, in line with the TG observations. The corresponding XPS patterns are illustrated in Fig. S5 and Table 3 for C 1s, with three types of carbon distinguishable. 1. Most of the contribution is from peak with binding energy of 284.8 eV arising from graphite carbon, which can be adventitiously introduced by contamination or in reaction, and is often used for calibration for the invariable nature. 2. Peaks centered at 283.9 eV can be ascribed to the presence of carbonaceous species that interact strongly with Ni surfaces, and are ascribed to Ni$_3$C, as Ni–C bond causes a shift to lower energies within 0.3 eV [69,70]. 3. The broad peak ranging from 288 to 291 eV originates from adsorbed CO$_3^{2-}$ interacting strongly with catalyst surface [40,71]. The carbonate is not stable at the reaction conditions, hence it is a product of surface adsorption in the postcatalytic handling when the spent catalysts are exposed to the open. It is seen that the Ni$_3$C portion increases with the introduction of Ag into Ni/CeO$_2$ system. It is still necessary to discriminate the graphite carbon by other means, because the chemical shift for C is invariable to different chemical environments.

O$_2$-TPO has been utilized as a complementary technique to determine the types of coke, and it is more pertinent than H$_2$-TPH technique, due to the fact that not all carbonaceous species can be gasified through methanation, but most coke are combustible. The O$_2$-TPO results are illustrated in Fig. 8. For all the samples, there is a small amount of O$_2$ consumption at the beginning of the oxidation process (<200 °C), which was due to the oxidation of metallic species such as Ni^0 or Ce^{3+} reduced under pretreatment with H$_2$ and the highly reducing reaction atmosphere. The assignment is justified because no CO or CO$_2$ has been observed from the effluent gas during the measurement at such low temperatures. For spent Ni/CeO$_2$, a broad O$_2$ consumption peak ranging from 350 to 600 °C centered at 520 °C is attributed to the combustion removal of deposited carbon. The asymmetric nature suggests that there are more than one type of carbon that are combusted, as oxidation of graphite and whisker carbon is almost indistinguishable in O$_2$-TPO measurement [4]. Intriguingly, one weak oxidation peak at 440 °C (C$_\alpha$) in addition to a shoulder peak at *ca.* 540 °C (C$_\beta$) is detected for Ni/CeO$_2$-3Ag and Ni/CeO$_2$-6Ag, which is confirmative to the TG results that the amount of coke deposition has been reduced by
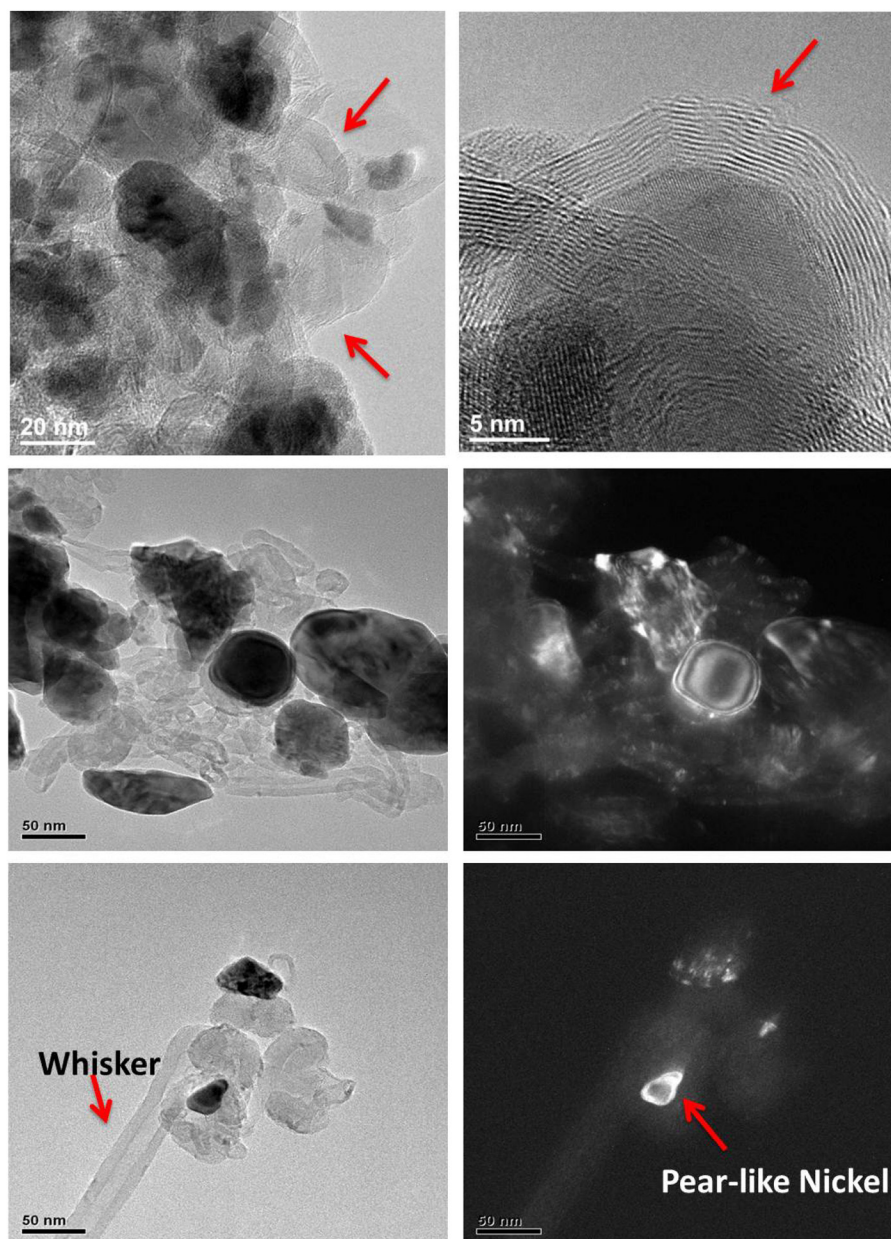
Fig. 9. TEM images of Ni/CeO$_2$ after the reaction under normal condition.

Ag, as shown in Fig. 8b and c, respectively. These results imply that there are two types of coke on the catalyst surface, and the low temperature one (C$_\alpha$) can be gasified easily than the other (C$_\beta$). While on the profile of Ni/CeO$_2$-24Ag, the 540 °C peak becomes virtually invisible as a result of negligible amount of coke, indicating that Ag changes the type of deposited coke from a recalcitrant C$_\beta$ to a more reactive C$_\alpha$. Here, from our O$_2$-TPO results, we conclude that the role of Ag is to reduce the amount of coke formed and alter the type of carbon to an easily gasifiable one.

TEM images of the spent catalysts are depicted in Figs. 9 and 10. For the spent Ni/CeO$_2$ catalyst, both whisker carbon and graphitic carbon can be identified, as indicated in the images by arrows. The whisker carbons are found in the vicinity of a pear-shaped Ni particle, as the shape of Ni particle changes with the reacting atmosphere, and pear-shaped Ni particles are important for the growth of whisker carbon [17]. Meanwhile, some encapsulating carbon with clear lattice fringes can also be seen, which is found to enclose the supported Ni particles (Fig. 9). In contrast, no whisker carbons are found in the spent Ni/CeO$_2$-3Ag, Ni/CeO$_2$-6Ag, or Ni/CeO$_2$-24Ag catalysts (Fig. 10). In Ni/CeO$_2$-3Ag, some encapsulated graphitic carbon covered on Ni catalyst surface is found, but no whisker carbon can be detected. Theoretical studies by Zhu et al. [20] have shown that Ag incorporation weakens the adsorption of *CH$_3$ or *CH$_2$, while enhances the adsorption of *CH or *C in the vicinity, and the formation of encapsulating carbon on Ni/CeO$_2$-3Ag is speculated to be reflective to this effect. As whisker carbon is a result of *C surface growth via diffusion [17], the absence of whisker carbon indicates that Ag inhibits the surface diffusion of *C on Ni surface. For Ni/CeO$_2$-6Ag, or Ni/CeO$_2$-24Ag, there is no clear evidence of either whisker carbon or encapsulating carbon, but only occasionally, pieces of carbon with blurred lattice fringe is identified (Fig. 10g). This is not surprising since Ag zoning or local absence can occur on the catalyst, and similar observations have been reported earlier [48]. Most of the coke deposited on Ag promoted catalysts is amorphous in nature. The absence of large numbers of whisker carbon and graphitic carbon gives direct
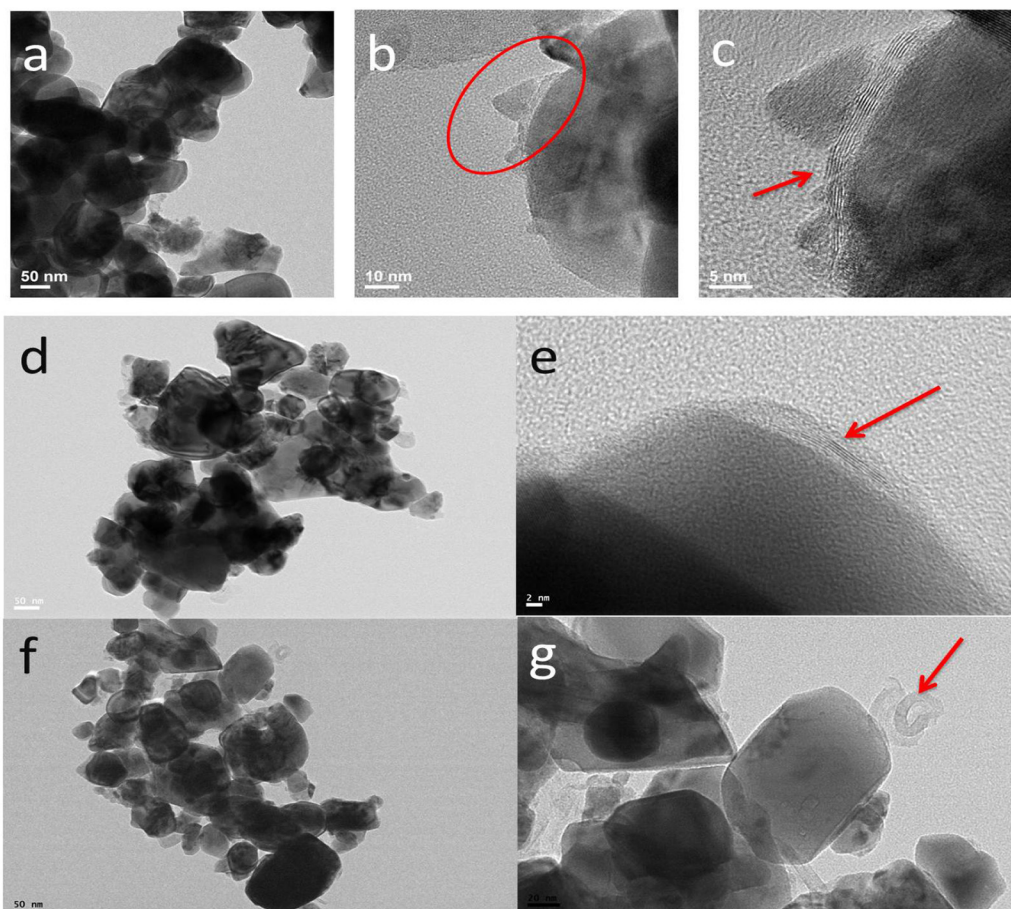
Fig. 10. TEM images of Ni/CeO$_2$-3Ag (a–c), Ni/CeO$_2$-6Ag (d and e), Ni/CeO$_2$-24Ag (f and g) after the reaction under normal condition.

evidence of inhibition of deposited carbon to nucleate and grow because of the presence of Ag, which is also corroborated by some previous studies [30,48]. These results are also consistent with the TG and O$_2$-TPO measurements.

3.4. Characterizations of spent catalysts under harsh condition

To understand the effect of reaction conditions on the amount of coke formed during DRM, TG and XRD are employed to measure the spent catalysts after 100 h time-on-stream under harsh conditions. The TG results displayed in Table 1 manifest that more than double amount of deposited carbon is found in the spent Ni/CeO$_2$ catalyst, indicating that carbon deposition is severe when stoichiometric feed is employed. For Ni/CeO$_2$-3Ag, 2.23 wt.% coke can be detected, but the amount of carbon on spent Ni/CeO$_2$-6Ag is comparable to the one under normal conditions, i.e., more Ag promoter is needed for the harsh reaction condition tests to suppress coke deposition. From the XRD patterns of spent catalysts shown in Fig. S6, a clear diffraction peak arising from (0 0 3) plane of graphitic carbon (JCPDS No. 26 - 1079) can be seen (pointed by asterisk), indicating a large amount of graphitic carbon that results from nucleation and growth on Ni surface. For the Ag promoted samples, no obvious difference can be identified from these tested under normal conditions, revealing that the introduction of Ag clearly minimizes carbon deposition in DRM even under harsh conditions.

3.5. Kinetic studies

To understand the effect of Ag from a kinetic viewpoint, we built up a differential reactor model [12,40] to explore the effect

of Ag on Ni/CeO$_2$ catalyst. Arrhenius curve is presented in Fig. 11 and the activation energies are listed in Table 4. Pristine Ni/CeO$_2$ gives activation energy of 91.0 kJ/mol, comparable with previously determined activation energies for unpromoted Ni catalysts for CH$_4$ activation. Wei and Iglesia [12] have deduced activation energy of 99–105 kJ/mol for Ni/Ni$_x$Mg$_{1-x}$O, and we have measured activation energy of 84.2 kJ/mol on reduced Ni/Ni$_{0.10}$Mg$_{0.90}$O (1 1 1) platelet catalyst [40], whereas 61 kJ/mol is obtained on Ni/YSZ catalyst [43]. The introduction of Ag clearly increases the activation energy to 144 kJ/mol, showing that the more reactive step sites on
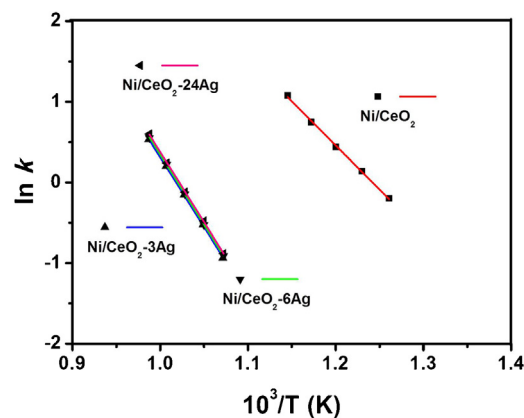

Fig. 11. Arrhenius plots of the CH$_4$ consumption rate obtained with the reactor operating under differential reaction condition for (a) Ni/CeO$_2$, (b) Ni/CeO$_2$-3Ag, (c) Ni/CeO$_2$-6Ag, and (d) Ni/CeO$_2$-24Ag.

Table 4
Activation energies of the catalysts.

| Catalysts	E_a (kJ/mol)
Ni/CeO$_2$	91.0
Ni/CeO$_2$-3Ag	143.8
Ni/CeO$_2$-6Ag	144.6
Ni/CeO$_2$-24Ag	144.8

Ni surface have been blocked. The fact that the surface alloy type catalyst increases the activation for reforming reactions has been observed before, and our result is in accordance with Sn [32,40] and Au [28]. The measured activation energies are found to be the same above 0.3 mol.% regardless of Ag loading, suggesting that almost the entire steps have been occupied with such a low Ag loading. The increase in activation energies by Ag introduction agrees with previous theoretical estimations proposed by Zhu et al. [20], whose results suggest that methane activation would be hindered by Ag. These authors also have recommended that Ag coverage on Ni surface can determine to which extent will the activation energy be elevated [20]. Such a prediction is not advocated by our experimental examination. Our measurements herein are different from previously deduced results. Neophytides et al. [43] have calculated an activation energy to be 61 kJ/mol for methane activation in internal steam reforming over Ni/YSZ, while increase to 115 and 137 kJ/mol for Ni(1Ag)/YSZ and Ni(5Ag)/YSZ. Their measurements are conducted via estimation of coking rate, as coking has the same activation energy with CH$_4$ reforming reactions, and CH$_4$ activation is the common rate-determine step [12,14] for both reactions. But once carbon deposition starts, the rate of coking is mainly controlled by carbon atom surface diffusion [17], thereby the activation energy does not reflect the steady state value for reforming reactions. Bueno et al. [30] have deduced that the apparent activation energies for Ag promoted Ni/Al$_2$O$_3$ in MSR are to increase continuously with Ag content. The reason for the discrepancy is still not well understood, and it is postulated that the difference may stem from the real loading of Ag on Ni surfaces. At low Ag loadings, Ag binds strongly to under-coordinated step sites on Ni surface, as corroborated by the elevation in activation energies. On the other hand, the excessive (with respect to the number of step sites on Ni surface) Ag presents at high loadings, Ag becomes highly mobile at high temperatures (>800 K)[26] and decorates virtually all the step sites. The interaction with terrace sites cannot be strong enough to accommodate Ag, and excessive Ag mainly resides on the CeO$_{2-x}$ support through surface diffusion from Ni surfaces. The Ag–CeO$_{2-x}$ interaction is also strong, especially under reducing atmosphere when CeO$_{2-x}$ becomes rich in oxygen vacancies, and can immobilize Ag clusters [59]. This speculation is also supported by the XPS measurement that Ag brings more surface vacancies on CeO$_2$ surface (Fig. 6 and Table 3), and also by the H$_2$-TPR patterns in Fig. 1.

The kinetic data also give information on the Ag–Ni interaction under reaction conditions. If the Ag–CeO$_2$ interaction is stronger than Ag–Ni attraction, Ag will bind strongly with CeO$_2$, resulting in the absence of Ag on Ni surfaces at low Ag loadings, for instance, for Ni/CeO$_2$-3Ag. The absence of Ag on Ni surface, in turn, will lead to an increase of activation energy close to that of pristine Ni/CeO$_2$. The observation that Ni/CeO$_2$-3Ag has identical activation energy to Ni/CeO$_2$-6Ag and Ni/CeO$_2$-24Ag corroborates that the Ag–Ni interaction is stronger than the Ag–CeO$_2$ interaction. Passivation of Ni surface by Ag coverage is also in line with the temperature-activity measurements depicted in Fig. 2. From the above inference, it is clear that Ag–Ni bonding is robust under the DRM reaction conditions. The interaction strength can be ordered as: Ag–Ni$_{step}$ > Ag–CeO$_{2-x}$ > Ag–Ni$_{terrace}$. On the other hand, excessive Ag on CeO$_2$ surface can be a reservoir to provide Ag atoms to Ni surface, and dynamically maintain the blockage of step sites over Ni surfaces.

3.6. Discussion

CeO$_2$ is well documented for the oxygen storage capacity that is associated with electron transformation between Ce^{3+} and Ce^{4+} [72]. CeO$_2$ has been employed as catalyst for Ni in reforming reactions, mainly for the purpose of coke removal via oxidation by oxygen anions. Ni/CeO$_2$ is a complicated system for the following features: 1. NiO dissolves into CeO$_2$ with a solubility between 10 and 12 mol.% [53], meaning that it is less likely to produce well dispersed reduced Ni^0 particles when Ni loading is well above this limit. The overloading can induce Ni^0 growth into big crystal particles that lose the coke-resistance properties, as a 26 wt.% Ni/CeO$_2$ has demonstrated to grow lots of whisker carbons as a result of Ni particle growth [45]. 2. Reduction of Ni/CeO$_2$ in H$_2$ can lead to the spread of Ni onto the support, as Ni^0 particle has demonstrated in *in situ* reduction atmosphere measurement [45]. Theoretical studies also suggest that CeO$_2$ surface can possess a metallic-like property when reduced, as a result of oxygen vacancy formation [73]. From these studies, one can expect that the reducing atmosphere can alter the wettability of Ni^0 on CeO$_2$ surfaces, as described in Sketch 1, resulting in an enlarged terrace area similar to Ni^0 growth. This could be the reason why when low loadings of Ni is charged, still large numbers of whisker carbons are visible under TEM measurements by previous researchers [44] and also by us. On the other hand, pristine Ni/CeO$_2$ has demonstrated robustness during methane reforming with CO$_2$ and O$_2$, as the atmosphere is oxidative and facilities oxidative removal of deposited coke [74]. 3. Meanwhile, under reducing atmosphere, Ni/CeO$_2$ undergoes surface reconstruction, where some tiny CeO$_2$ moieties migrates onto Ni surface and buries the Ni inside CeO$_2$ bulk, resulting in a reduced surface area of metallic Ni^0 [58]. As the structure of Ni/CeO$_2$ under DRM reaction condition is similar to the reducing conditions [45], the complicated morphology can induce deactivation and coke formation. In our catalytic tests, we have observed a fast deactivation when H$_2$ is co-fed, which strongly indicates that the atmosphere composition does affect the
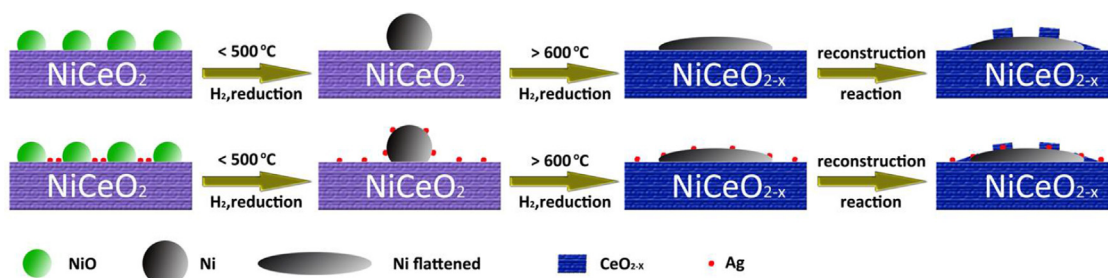
Sketch 1. The Ni/CeO$_2$ and Ni/CeO$_2$-xAg morphology variation with respect to contacting atmosphere.

structure of Ni^0 for the above reasons. Though CeO_2 or other oxygen conductor materials have been proposed as ideal choice for alkane reforming reactions for their OSC property, here we argue that the choice of support may depend on the reaction atmosphere. CeO_2 is reducible and can lead to the formation of surface vacancies, which is predicated to make the surface metallic-like. Actually, reduced CeO_2 can change the wettability to supported metals dynamically, resulting in the formation of large areas for Ni terraces [45]. An enlarged terrace favors nucleation and growth of deposited coke, as the two dimensional flake-like graphene is energetically stabilized by larger terrace areas [14]. Hence, pristine Ni/CeO_2 may not be an ideal coke-resistant catalyst under reducing reaction conditions such as DRM.

Ag as a promoter has been proposed by Nørskov et al. [29] and shown to enhance the long term stability via forming surface alloys. Ag tends to nucleate on the step sites of Ni surface, leading to the formation of Ag islands [26]. But the mobility of Ag can be enhanced upon heating above 800 K, resulting in complete blockage of steps [26,29]. Herein, we demonstrate that the same concept also works in DRM for Ag promoted Ni/CeO_2 catalysts. The promoting effect is found to be unaffected by H_2 co-feeding, showing that the Ag–Ni interaction is stronger than Ag–CeO_2 interaction even under reducing atmosphere, which is also confirmed by the kinetic measurement that activation energy increases by Ag. The surface composition for spent catalysts shows that surface concentration of Ag is not prominently higher than that in the bulk, suggesting that both Ni and Ag are embedded into CeO_2, presumably by the burial effect caused by CeO_2 migration (Sketch 1).

Besides the inhibition role in coke deposition, Ag also accelerates the combustion of deposited coke. The promoting role in gasification of coke may be two folds. In the first place, Ag destabilizes the formed coke by inhibiting the nucleation and growth of deposited coke, hence far less graphitic or whisker carbons are produced over Ag promoted Ni. Therefore, amorphous carbon species, which is easy to be gasified as manifested by the O_2-TPO measurements for the spent catalysts, dominate on Ag promoted Ni catalysts. In the second place, Ag is permeable to oxygen species and is capable of dissolving oxygen in the crystalline matrix [75]. From the spent Ag promoted catalyst, a given amount of Ag^+ is detected by XPS, strongly supporting this reasoning. In this respect, the seemingly excessive loading of Ag above 0.3 mol.% is also important for the gasification of coke.

4. Conclusions

The effect of Ag on the stability of Ni/CeO_2 in methane carbon dioxide dry reforming has been explored, under varied temperatures from 560 to 760 °C and different feedstock conditions. On pristine Ni/CeO_2 catalyst, the formation of whisker and encapsulating graphitic carbon and surface reconstruction cause slow and continuous deactivation. The deactivation process is aggravated when H_2 is co-fed or during carrier-gas free conditions for pristine Ni/CeO_2 catalyst. Ag significantly reduces the intrinsic activity of Ni surfaces as a result of activation energy increase, and simultaneously enhances the long term (100 h) stability under various feedstock conditions. 3 mol.% of Ag is enough to cover all the under-coordinated step sites on Ni surface, and excessive Ag will migrate and bind with CeO_{2-x} support. Ag lowers the content of coke and switches the type of formed coke from whisker carbon or graphitic carbon to amorphous carbon. The role of Ag is to restrain coke nucleation and growth into whisker or graphitic carbon, and to stimulate gasification of deposited coke on the catalyst surface. As the Ni/CeO_2 catalyst also undergoes surface reconstruction, a slow deactivation caused by surface composition or structure is also observed for Ag promoted samples.

Appendix A. Supplementary data

Supplementary material related to this article can be found, in the online version, at http://dx.doi.org/10.1016/j.apcatb.2014.09.066.

References

[1] A.T. Ashcroft, A.K. Cheetham, M.L.H. Green, P.D.F. Vernon, Nature 352 (1991) 225–226.
[2] C. Liu, J. Ye, J. Jiang, Y. Pan, ChemCatChem 3 (2011) 529–541.
[3] Y.H. Hu, Advances in CO_2 Conversion and Utilization, American Chemical Society, 2010, pp. 155–174.
[4] W. Chen, G. Zhao, Q. Xue, L. Chen, Y. Lu, Appl. Catal. B 136–137 (2013) 260–268.
[5] J.R. Rostrup-Nielsen, S. Jens, J.K. Nørskov, in: H.K. Bruce Gates (Ed.), Advances in Catalysis, 2nd ed., Academic Press, New York, 2002, pp. 65–139.
[6] G.A. Olah, A. Goeppert, M. Czaun, G.K. Prakash, J. Am. Chem. Soc. 135 (2013) 648–650.
[7] J.T. Richardson, S.A. Paripatyadar, Appl. Catal. 61 (1990) 293–309.
[8] S. Wang, G.Q. Lu, G.J. Millar, Energy Fuels 10 (1996) 896–904.
[9] J. Petrasch, J. Klausner, Wiley Interdisciplinary Rev.: Energy Environ. 1 (2012) 347–361.
[10] C. Agrafiotis, H. von Storch, M. Roeb, C. Sattler, Renew. Sust. Energ. Rev. 29 (2014) 656–682.
[11] S. Gaur, D.J. Haynes, J.J. Spivey, Appl. Catal. A 403 (2011) 142–151.
[12] J. Wei, E. Iglesia, J. Catal. 224 (2004) 370–383.
[13] G. Jones, J.G. Jakobsen, S.S. Shim, J. Kleis, M.P. Andersson, J. Rossmeisl, F. Abild-Pedersen, T. Bligaard, S. Helveg, B. Hinnemann, J.R. Rostrup-Nielsen, I. Chorkendorff, J. Sehested, J.K. Nørskov, J. Catal. 259 (2008) 147–160.
[14] H.S. Bengaard, J.K. Nørskov, J. Sehested, B.S. Clausen, L.P. Nielsen, A.M. Molenbroek, J.R. Rostrup-Nielsen, J. Catal. 209 (2002) 365–384.
[15] D.L. Trimm, Catal. Today 49 (1999) 3–10.
[16] N.A. Jarrah, J.G. van Ommen, L. Lefferts, J. Catal. 239 (2006) 460–469.
[17] S. Helveg, C. Lopez-Cartes, J. Sehested, P.L. Hansen, B.S. Clausen, J.R. Rostrup-Nielsen, F. Abild-Pedersen, J.K. Nørskov, Nature 427 (2004) 426–429.
[18] J. Rostrup-Nielsen, J. Nørskov, Top. Catal. 40 (2006) 45–48.
[19] E. Nikolla, J. Schwank, S. Linic, J. Catal. 250 (2007) 85–93.
[20] Y. Xu, C. Fan, Y.-A. Zhu, P. Li, X.-G. Zhou, D. Chen, W.-K. Yuan, Catal. Today 186 (2012) 54–62.
[21] J. Gao, J. Yip, J. Zhao, B.I. Yakobson, F. Ding, J. Am. Chem. Soc. 133 (2011) 5009–5015.
[22] S. Saadi, F. Abild-Pedersen, S. Helveg, J. Sehested, B. Hinnemann, C.C. Appel, J.K. Nørskov, J. Phys. Chem. C 114 (2010) 11221–11227.
[23] S. Helveg, J. Sehested, J.R. Rostrup-Nielsen, Catal. Today 178 (2011) 42–46.
[24] Y.H. Hu, E. Ruckenstein, Catal. Rev. Sci. Eng. 44 (2002) 423–453.
[25] J.R. Rostrup-Nielsen, Chem. Eng. Sci. 50 (1995) 4061–4071.
[26] J.V. Lauritsen, R.T. Vang, F. Besenbacher, Catal. Today 111 (2006) 34–43.
[27] A.V. Ruban, H.L. Skriver, J.K. Nørskov, Phys. Rev. B 59 (1999) 15990–16000.
[28] F. Besenbacher, I. Chorkendorff, B.S. Clausen, B. Hammer, A.M. Molenbroek, J.K. Nørskov, I. Stensgaard, Science 279 (1998) 1913–1915.
[29] R.T. Vang, K. Honkala, S. Dahl, E.K. Vestergaard, J. Schnadt, E. Laegsgaard, B.S. Clausen, J.K. Norskov, F. Besenbacher, Nat. Mater. 4 (2005) 160–162.
[30] N.V. Parizotto, K.O. Rocha, S. Damyanova, F.B. Passos, D. Zanchet, C.M.P. Marques, J.M.C. Bueno, Appl. Catal. A 330 (2007) 12–22.
[31] E. Nikolla, J. Schwank, S. Linic, J. Am. Chem. Soc. 131 (2009) 2747–2754.
[32] E. Nikolla, J. Schwank, S. Linic, J. Catal. 263 (2009) 220–227.
[33] O. Yamazaki, T. Nozaki, K. Omata, K. Fujimoto, Chem. Lett. 21 (1992) 1953–1954.
[34] T. Horiuchi, K. Sakuma, T. Fukui, Y. Kubo, T. Osaki, T. Mori, Appl. Catal. A 144 (1996) 111–120.
[35] Y. Wang, H. Wang, Y. Li, Q. Zhu, B. Xu, Top. Catal. 32 (2005) 109–116.
[36] Y.H. Hu, Catal. Today 148 (2009) 206–211.
[37] L. Yang, Y. Choi, W. Qin, H. Chen, K. Blinn, M. Liu, P. Liu, J. Bai, T.A. Tyson, M. Liu, Nat. Commun. 2 (2011) 357.
[38] G.A. Olah, G.K.S. Prakash, A. Goeppert, M. Czaun, T. Mathew, J. Am. Chem. Soc. 135 (2013) 10030–10031.
[39] H. Xiao, Z. Liu, X. Zhou, K. Zhu, Catal. Commun. 34 (2013) 11–15.

[40] M. Yu, K. Zhu, Z. Liu, H. Xiao, W. Deng, X. Zhou, Appl. Catal. B 148–149 (2014) 177–190.
[41] O. Yamazaki, K. Tomishige, K. Fujimoto, Appl. Catal. A 136 (1996) 49–56.
[42] H.-S. Roh, H.S. Potdar, K.-W. Jun, Catal. Today 93–95 (2004) 39–44.
[43] I. Gavrielatos, D. Montinaro, A. Orfanidi, S.G. Neophytides, Fuel Cells 9 (2009) 883–890.
[44] X. Du, D. Zhang, L. Shi, R. Gao, J. Zhang, J. Phys. Chem. C 116 (2012) 10009–10016.
[45] V.M. Gonzalez-DelaCruz, J.P. Holgado, R. Pereñíguez, A. Caballero, J. Catal. 257 (2008) 307–314.
[46] T. Odedairo, J. Chen, Z. Zhu, Catal. Commun. 31 (2013) 25–31.
[47] W. Xu, Z. Liu, A.C. Johnston-Peck, S.D. Senanayake, G. Zhou, D. Stacchiola, E.A. Stach, J.A. Rodriguez, ACS Catal. 3 (2013) 975–984.
[48] A.K. Rovik, S.K. Klitgaard, S. Dahl, C.H. Christensen, I. Chorkendorff, Appl. Catal. A 358 (2009) 269–278.
[49] H. Jeong, M. Kang, Appl. Catal. B 95 (2010) 446–455.
[50] Y.-A. Zhu, D. Chen, X.G. Zhou, P.O. Astrand, W.K. Yuan, Surf. Sci. 604 (2010) 186–195.
[51] W. Deng, X. Wang, F. Jiao, K. Zhu, J. Nanopart. Res. 15 (2013) 1–10.
[52] J.G. Zhang, H. Wang, A.K. Dalai, J. Catal. 249 (2007) 300–310.
[53] L. Barrio, A. Kubacka, G. Zhou, M. Estrella, A. Martiínez-Arias, J.C. Hanson, M. Fernaíndez-Garciía, J.A. Rodriguez, J. Phys. Chem. C 114 (2010) 12689–12697.
[54] S. Chang, M. Li, Q. Hua, L. Zhang, Y. Ma, B. Ye, W. Huang, J. Catal. 293 (2012) 195–204.
[55] Y. Yang, S. Lim, G. Du, Y. Chen, D. Ciuparu, G.L. Haller, J. Phys. Chem. B 109 (2005) 13237–13246.
[56] A. Parmaliana, F. Arena, F. Frusteri, N. Giordano, J. Chem. Soc. Faraday Trans. 86 (1990) 2663–2669.
[57] A.E. Castro Luna, M.E. Iriarte, Appl. Catal. A 343 (2008) 10–15.
[58] A. Caballero, J.P. Holgado, V.M. Gonzalez-delaCruz, S.E. Habas, T. Herranz, M. Salmeron, Chem. Commun. 46 (2010) 1097–1099.
[59] J.A. Farmer, C.T. Campbell, Science 329 (2010) 933–936.
[60] D. Alders, F.C. Voogt, T. Hibma, G.A. Sawatzky, Phys. Rev. B 54 (1996) 7716–7719.
[61] A.F. Carley, S.D. Jackson, J.N. O'Shea, M.W. Roberts, Phys. Chem. Chem. Phys. 3 (2001) 274–281.
[62] L. Guczi, G. Stefler, O. Geszti, I. Sajó, Z. Pászti, A. Tompos, Z. Schay, Appl. Catal. A 375 (2010) 236–246.
[63] P. Prieto, V. Nistor, K. Nouneh, M. Oyama, M. Abd-Lefdil, R. Díaz, Appl. Surf. Sci. 258 (2012) 8807–8813.
[64] K. Zhou, X. Wang, X. Sun, Q. Peng, Y. Li, J. Catal. 229 (2005) 206–212.
[65] D. Kong, G. Wang, Y. Pan, S. Hu, J. Hou, H. Pan, C.T. Campbell, J. Zhu, J. Phys. Chem. C 115 (2011) 6715–6725.
[66] J. Rodriguez, Surf. Sci. 296 (1993) 149–163.
[67] J. Shu, B.E.W. Bongondo, B.P.A. Grandjean, A. Adnot, S. Kaliaguine, Surf. Sci. 291 (1993) 129–138.
[68] A. Nagy, G. Mestl, Appl. Catal. A 188 (1999) 337–353.
[69] C. Bittencourt, A. Felten, J. Ghijsen, J.J. Pireaux, W. Drube, R. Erni, G. Van Tendeloo, Chem. Phys. Lett. 436 (2007) 368–372.
[70] P.M. Blass, S. Akhter, C.M. Seymour, J.J. Lagowski, J.M. White, Surf. Sci. 217 (1989) 85–102.
[71] H. Onishi, C. Egawa, T. Aruga, Y. Iwasawa, Surf. Sci. 191 (1987) 479–491.
[72] H.-P. Zhou, H.-S. Wu, J. Shen, A.-X. Yin, L.-D. Sun, C.-H. Yan, J. Am. Chem. Soc. 132 (2010) 4998–4999.
[73] S. Fabris, G. Vicario, G. Balducci, S. de Gironcoli, S. Baroni, J. Phys. Chem. B 109 (2005) 22860–22867.
[74] S. Xu, X. Yan, X. Wang, Fuel 85 (2006) 2243–2247.
[75] A. Nagy, G. Mestl, T. Rühle, G. Weinberg, R. Schlögl, J. Catal. 179 (1998) 548–559.